SPACE PROPULSION 2022

ESTORIL, PORTUGAL | 09 – 13 MAY 2022

Testing the NANO AR³ FEEP cubesat electric propulsion system at ESA Propulsion Laboratory

Martin Eizinger [(1)], José Gonzalez del Amo [(2)], Luca Bianchi [(2)], Davina Di Cara [(2)],
Quirin Koch [(3)], David Krejci [(3)], Alexander Reissner [(3)], Kaarel Repän [(3)], Tony Schönherr [(3)]

[(1)(2)] *European Space Agency (ESTEC), Noordwijk, The Netherlands, Email: martin.eizinger@esa.int*
[(3)] *ENPULSION GmbH, Wiener Neustadt, Austria, Email: tony.schoenherr@enpulsion.com*

KEYWORDS: field emission electric propulsion, thrust vectoring, characterisation, indium, Faraday cup, ESA R&D, TDE

ABSTRACT:

Space propulsion systems undergo thorough ground testing before being deployed in space. We report the results of a functional verification and performance characterisation test campaign of an integrated electric propulsion system for cubesats and microsats with purely electric thrust vectoring capability and no moving parts.

Visualisations of the plume data obtained from Faraday cup scans show a clear, corresponding trend of the variation of the inclination and azimuth angles of the thrust vector when these are commanded.

The divergence angle computed from plasma diagnostic data is 49°, independently of the achieved inclination of the ion beam.

1. INTRODUCTION

This paper is based on an experimental verification of the thrust vectoring capability of the DUT.

1.1. Thrust vectoring

Adjustability of the thrust vector of a space propulsion system is a highly valuable feature. Depending on the configuration of the propulsion system on the spacecraft, it allows not only for more advanced orbital manoeuvres but also for introducing a torque. Furthermore, a propulsion system can develop an undesired inclination of the thrust vector over its lifetime or even present one at beginning of life (BOL) despite strict manufacturing tolerances, depending on the technology, e.g. [1], [2]. This can be compensated only with the ability to adjust the thrust vector.

Many approaches for thrust vectoring can be identified. A very low-resolution example is the use of multiple, spatially separated and selectively activated thrusters. An asymmetry of the exhaust plumes naturally results in an off-centred thrust [2]. If the bases of the thrusters are not coplanar, the vector sum is also inclined with respect to the spacecraft coordinate system.

A different approach is to mechanically change the orientation of one or more thrusters, which naturally brings about an inclined thrust vector. Due to the complexity of bearings compliant with the environment of outer space, intricate designs using compliant mechanisms have been presented that provide rigid rotation of nozzles around two axes [3]. Another possibility to achieve an inclined thrust vector is by injecting a secondary flow that diverts the main flow away from the geometric axis [4].

In contrast to the exhaust gas of chemical propulsion systems, electric propulsion (EP) systems have an additional mechanism for applying forces or torques to the propellant, i.e. the electric charge of the exhaust particles. In fact, that is how most EP technologies produce thrust in the first place, however commonly the resulting force of the electric or magnetic field is collinear with the geometrical axis of the thruster.

The device under test (DUT) for which data are presented in this paper is categorised as an electrostatic propulsion system. As such, the thrust it produces is the reaction to the electrostatic force applied to the ionised atoms in the exhaust plume. By modifying the electric field to not be axisymmetric, the ions experience an acceleration component in radial direction, resulting in an overall inclined thrust vector.

1.2. Device under test

The NANO AR³ is a fully integrated propulsion system developed by ENPULSION in cooperation with FOTEC in the frame of the ESA Technology Development Element (TDE) project "*Innovative Propulsion systems for Cubesats and Microsats*". It is a derivative of the flight-proven Indium FEEP Multiemitter (IFM) NANO (now commercially called "ENPULSION NANO"), which was first deployed in space in 2018 [5][6] after over 20 years of collaborative development between FOTEC and the

European Space Agency (ESA) [7][8][9][10][11]. Since then, several new variants of the product have been in development, including the NANO AR³, whose primary attribute is its thrust vectoring capability.

The NANO AR³, the device under test, is an indium Field-Emission Electric Propulsion (FEEP) system with a crown emitter and a segmented extractor, two neutralisers and a Power Processing Unit (PPU). The system provides controllable thrust between 100 and 350 µN, at a specific impulse greater than 2000 s and with a power consumption lower than 45 W. The underlying electric parameters are entirely controlled by the on-board embedded firmware through calibrated algorithms that take the target angles as input.

1.2.1. Basic functionality

During operation and stand-by, the propellant is in the liquid phase. Capillary forces transport it from the reservoir to the expulsion area, which is a circular configuration of 28 small needles, usually referred to as the crown. The crown is part of the emitter-subassembly, and entirely wetted with the propellant, which is indium. It is furthermore surrounded by the extractor ring, which in case of the AR³ is split into three segments. Fig.1 shows this arrangement from an external view of the final assembly.

Figure 1: Close-up of emitter and extractor configuration of the NANO AR³

During nominal operation, the extractors are at a high negative potential, while the emitter is at a high positive potential. The resulting electric field applies a stress to the liquid, electrically conductive propellant, which consequently deforms at the needle tips into a shape known as a Taylor cone [12]. At sufficiently high voltages, a jet of liquid starts to emanate from the apex of the Taylor cone [12], and the ions within it are accelerated by the electric field. Varying the potential across the extractor segments causes an asymmetric electric field and consequently a radial component of acceleration.

Independent control of the extractor segments requires additional electronics compared to the model with a single extractor.

1.2.2. Propellant

Unlike the most common propellants, indium is not a gas at room temperature. This, along with some other differences to noble gases, makes it convenient in many ways for use as a propellant. However, it also leads to effects that need to be considered in testing. For example, Mühlich et al. developed an advanced design of Faraday cups for ion current measurement, which is highly accurate and specifically suitable for indium FEEP ion sources [13].

1.3. Test objective

The objective of the test is to characterise the thrust vectoring capability of the DUT. This is achieved by commanding several combinations of inclination and azimuth and qualitatively comparing visualisations of the Faraday scans of these operating points (OPs). The combinations of inclination and azimuth of all inclined thrust vector operating points are listed in Tab.1. The thrust value varies based on inclination, namely 349 µN, 299 µN, and 249 µN for 5°, 10°, and 12.5° respectively.

Table 1: Inclination and azimuth for all operating points

Incl	Az	Incl	Az	Incl	Az
5°	0°	10°	30°	12.5°	0°
5°	60°	10°	90°	12.5°	60°
5°	120°	10°	150°	12.5°	120°
5°	180°	10°	210°	12.5°	180°
5°	240°	10°	270°	12.5°	240°
5°	300°	10°	330°	12.5°	300°

2. METHODS

The main methods for obtaining test data are plasma diagnostics, telemetry from the DUT, and basic data from ground support equipment (GSE).

2.1. Test facility

The test is carried out in the SPF vacuum facility at the ESA Propulsion Laboratory (EPL) of the European Space Research and Technology Centre (ESTEC). The main vacuum chamber has a diameter of 2 m and a length of 2 m. High vacuum is mainly achieved with a turbomolecular pump. The cryogenic pumping systems of the facility are not used, because of the propellant's tendency of sticking to surfaces already at room temperature.

2.2. Plasma diagnostics

In this test, all plasma data are obtained using Faraday cups (FCs). Measurements are acquired at multiple elevation angles (up and down relative to the chamber axis) and sweep angles (left and right relative to the chamber axis) to achieve a high resolution of the ion beam. This is realised by a semi-circular arm that holds FCs and can rotate around a vertical axis (schematic see Fig.2).
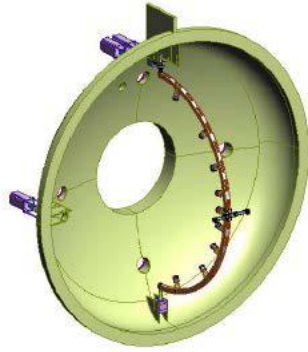
Figure 2: Exemplary scheme of SPF's diagnostic arm with Faraday cups

In total, twelve FCs are used to resolve the elevation from -72° to 72°, while the sweep angle reaches from -70° to 70° with approximately 3° resolution. The FCs are distributed asymmetrically to allow for placement of one probe at 0° despite the use of an even number of probes. The position of all probes is summarised in Tab.2.

Table 2: Angular position of Faraday probes with respect to the horizontal plane

ID	angle	supplier	ID	angle	supplier
1	-72	FOTEC	12	72	FOTEC
2	-54	FOTEC	11	54	FOTEC
3	-36	FOTEC	10	36	FOTEC
4	-24	FOTEC	9	24	FOTEC
5	-12	FOTEC	8	12	ALTA/ SITAEL
6	-6	FOTEC	7	0	FOTEC

Two different implementations of FCs are used. More specifically, all but one probe are specifically designed for use with indium (FOTEC probes). The twelfth probe's design is based on noble gases as propellants (ALTA/SITAEL probe). This is to gain information about the validity of the probe designs. Comparability is enabled by placing the ALTA probe at a location symmetric to one of the FOTEC probes (specifically 12° and -12°, respectively). Fig.3 shows one specimen of each probe.
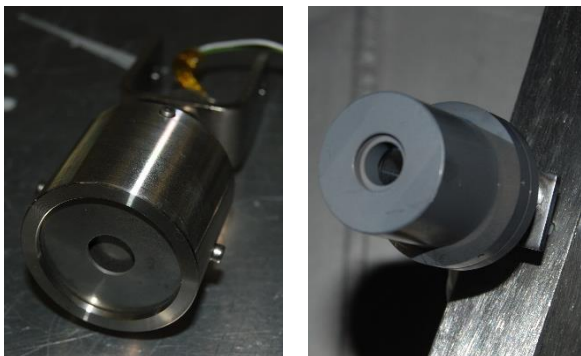
Figure 3: Faraday probes (left: ALTA, right: FOTEC)

The FCs have a collector and a shield, biased at -20 V, and +10 V respectively.
Data from these probes are acquired in sets called "scans", where one scan is one sweep of the arm. Each scan is stored in a dedicated log file.

2.3. Telemetry

The DUT communicates with the electronic GSE (EGSE) and transmits a wide range of data such as housekeeping (e.g. bus voltage and current, software fuses, temperature of critical components) and operational quantities (e.g. internal voltages, thrust derived from a mathematical model, thrust vector angles).
The software on the EGSE computer makes these data graphically available to the user and also stores them in one continuously acquired log file, split over time for different test segments.

2.4. Ground support equipment

Apart from the DUT-dedicated software, the EGSE computer runs a software to acquire GSE-related data and to supply the DUT with power. The DUT is connected to a laboratory power supply that simulates the spacecraft bus. In addition, the variant tested in this campaign has an integrated relay that serves as an on-off switch, allowing for switch-off of the device without disabling the bus voltage. A separate power supply provides the voltage for this relay.
The GSE also measures the temperature at multiple locations outside of the DUT, including the temperature reference point (TRP) used for simulation-based thermal analyses. In addition, the pressure inside the facility measured with vacuum gauges is recorded by the software. Similarly to the telemetry, these data are acquired continuously, but unlike the DUT telemetry, the data are not split into test-specific segments.

3. DATA PROCESSING

Diagnostic data are processed in multiple steps before analysis and presentation. Because these steps are carried out independently by two parties (ESA and ENPULSION), they are described generically rather than with the explicit or computational operations.

3.1. Axial offset correction

The location on the DUT from which ions are extracted does not coincide with the centre of the semi-circular arrangement of probes. Instead, an offset in axial direction is present as a consequence of facility-related technical limitations. This results in multiple geometrical effects that need to be corrected for.

3.1.1. Different distances of the probes

The effective distance from the location of ion expulsion to each probe depends on both the elevation angle of the probe and the sweep angle. The offset can simply be added to the radius of the arm if elevation and sweep angle are both equal to

zero (i.e. central probe directly in front of the DUT). For all other sweep angles, a triangular summation applies. This triangle only lies in the plane of the sweep angle for the central probe; for all other probes, both angles must be considered (see Fig.4).
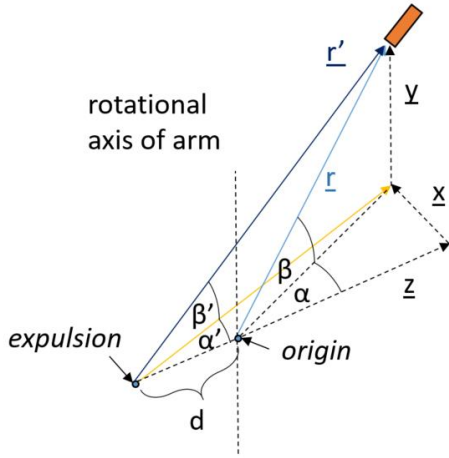
Figure 4: Effect of a displacement "d" on the perceived distances and angles of a probe

The distance between the diagnostic arm structure and the probe collimators is assumed constant for all probes. This approach neglects the slight variation resulting from the non-radial orientation of non-central probes because they are aimed at the offset point. The final value of the distance is obtained by taking the absolute of the position vector of the probe after adding the displacement to the z component as in Eq.1.

$$\underline{r}' = \begin{pmatrix} x \\ y \\ z + d \end{pmatrix} \qquad \text{Eq.1}$$

The components are calculated from the arm radius, its position, and the mounting position of the probe (see Fig.4):

$$x = r \cdot \cos(\beta) \cdot \sin(\alpha) \qquad \text{Eq.2}$$
$$y = r \cdot \sin(\beta) \qquad \text{Eq.3}$$
$$z = r \cdot \cos(\beta) \cdot \cos(\alpha) \qquad \text{Eq.4}$$

3.1.2. Narrowing of angles

Both elevation and sweep angle are initially measured with respect to the centre of the arm. To convert them to the angles as seen from the location of ion expulsion, the angles α' and β' of the triangles described in the previous paragraph are applicable. Their computation follows from Eq.2, Eq.3, and Eq.4 using simple trigonometry.

3.1.3. Shadowing of the collimator

Another effect of the aforementioned displacement is that the collimator of the probes appears as an ellipse rather than as a circle from the point of view of the location of expulsion. The vertical component of this effect, i.e. the shadowing pertaining to the elevation of the probes, is addressed by performing a laser alignment procedure prior to acquisition. However, because the offset also applies to the rotational axis of the arm, this distortion of the

collimator also occurs for the sweep angle. This results in a reduced intake area of the probe. Knowing the area perpendicular to the direction of motion of the ions is critical for correctly computing the ion current density. Fig.5 shows three examples of such a distortion (note that the vectors $\underline{x}$, $\underline{y}$, and $\underline{z}$ are to be treated separately for each scenario, i.e. even though $\underline{z}_3$ and $\underline{z}_2$ are drawn the same, they would not have the same length for position 2 and 3 of any given probe).
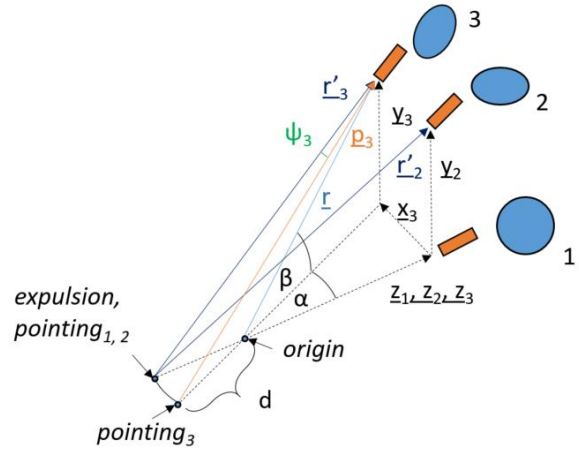
Figure 5: Effect of a displacement "d" on the apparent shape of the collimator (blue) illustrated on the example of three different probe locations (1: central probe at 0°, 2: elevated probe at 0°, 3: elevated probe at arbitrary nonzero angle)

Shadowing effects due to the thickness of the collimator disc are neglected in this analysis. The area relevant for the calculation of the current density is the area of the ellipse, which is calculated as $A = \pi \cdot a \cdot b$, where a is simply the radius of the collimator and b is equal to the radius shortened by the cosine of the angle ψ between the normal vector of the collimator ($\underline{p}$) and the position vector from the expulsion point to the probe ($\underline{r}'$). Because the pointing of all probes to the offset point is performed when the arm is at the centre, the normal vector $\underline{p}$ can be computed from the ideal position vector $\underline{r}$ of the probe (which results directly from the arm radius, sweep angle, and elevation angle) by adding the x and z components of the length d rotated by the sweep angle. Finally taking the scalar product of these two vectors yields the factor by which b is shorter than the radius. The area of the visible ellipse is thus calculated as

$$A_{ellipse} = A_{circ} \cdot \frac{\underline{p} \cdot \underline{r}'}{|\underline{p}| \cdot |\underline{r}'|} \qquad \text{Eq.5}$$

with the pointing vector according to Eq.6 and the position vector according to Eq.1.

$$\underline{p} = \begin{pmatrix} x + d \cdot \sin(\alpha) \\ y \\ z + d \cdot \cos(\alpha) \end{pmatrix} \qquad \text{Eq.6}$$

3.2. Scaled current density

The aforementioned correction terms as well as scaling based on distance and area are applied to

the raw currents according to Eq.7, eventually yielding the current density scaled to a certain distance r from the DUT.

$$j_{DuT}(\alpha', \beta') = \frac{i_{raw}(\alpha, \beta)}{A_{ellipse}} \cdot \frac{|\underline{r}'|^2}{|\underline{r}|^2} \qquad \text{Eq.7}$$

Note that the indexes "DUT" and "raw" imply the transformation of angles as described.

This computation assumes that the trajectory of ions from the point of expulsion to the FC collimator is a straight line.

3.3. Averaging

Multiple Faraday scans over the whole range of sweep and elevation angles are performed for each operating point (OP), where an OP is characterised by a unique combination of thrust magnitude, thrust vector inclination, and thrust vector azimuth. The data of these scans is averaged into one matrix per operating point.

3.4. Interpolation

The matrix of scaled current densities for a single OP is fed to a Clough-Tocher 2D interpolation algorithm [14], which facilitates smoothly plotting the data as well as integrating in a spherical coordinate system. The domain of the resulting 2D field is given by the extrema of the corrected sweep and probe angles, i.e. two pairs of values.

3.5. Conversion to DUT coordinate system

From the point of view of the DUT, a spherical coordinate system of zenith and azimuth is more intuitive than a system of elevation and sweep angle. This is particularly relevant for the computation of the divergence angle. Fig.6 shows the coordinate system into which the data are transformed.
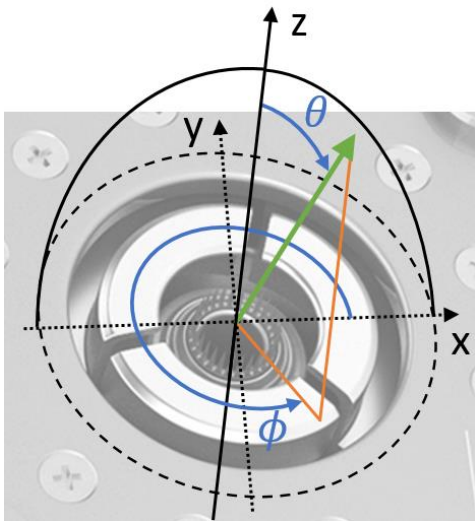
Figure 6: Spherical coordinate system centred at the expulsion point of the device under test and aligned with the device's Cartesian coordinate system

If the interpolated field is described using this coordinate system, the definition of its domain changes slightly: the two pairs of limits become, for simplicity, one single limit describing the maximum zenith angle where the field is defined at all azimuthal angles. This maximum zenith angle θ_{max} is the minimum of the absolute values of the four limits of the original interpolated field.

The aforementioned coordinate transformation is not performed for the presentation of the raw FC measurements; instead, these are plotted as the raw current over the (corrected) sweep angle.

3.6. Divergence angle

The divergence angle is computed based on the total current and consequently relies on a summation over the interpolation field. This is done in spherical coordinates, where the limits of integration are ideally such that a hemisphere is covered. However, the zenith angle is limited to approximately 60° as a result of the range of the interpolation field.

The mathematical formulation for the integral of the current density is shown in Eq.8, where the product of the two terms in parentheses describes the area of a surface element.

$$i = \int_0^{\theta_1} \int_0^{2\pi} j \cdot (R \sin(\theta)\, d\phi) \cdot (R\, d\theta) \qquad \text{Eq.8}$$

However, because the integration is carried out numerically, discrete steps of $d\phi$ and $d\theta$ are taken, causing a small error because the upper edge of the surface element is shorter than the lower edge. To minimise the impact of this error, the values for the current density are taken at the centre of each discrete step rather than at its edge. The first value is therefore not taken at $\theta = 0$ like the integral indicates, but at $\theta = \frac{\Delta\theta}{2}$, where $\Delta\theta$ is the step size.

This integral is taken once for $\theta_1 = \theta_{max}$ to determine the total current (at least within the domain of the data), and then once again with a break-condition when 95% of the total current is reached. The angle where this condition is reached is taken as the divergence angle, equal to the half-angle of the spherical sector whose cap accounts for (at least) 95% of the total ion current.

3.7. Measurement offset correction

Performing a scan with the acquisition system on but with the DUT off (i.e. with no plasma present) shows a highly stable nonzero signal (see Fig.7).
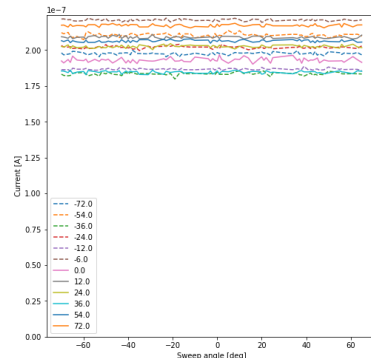
Figure 7: Current measurements without plasma

This is likely a product of the measurement electronics, caused by an input offset voltage or an input bias current through the shunt. If this offset is assumed to be independent of the amplitude of the signal, it can simply be subtracted from the measurement. Fig.8 shows data from one scan, with and without the offset subtracted. More specifically, the signals shown in Fig.7 are averaged over the sweep angle, and these averages are subtracted from the corresponding channel data.
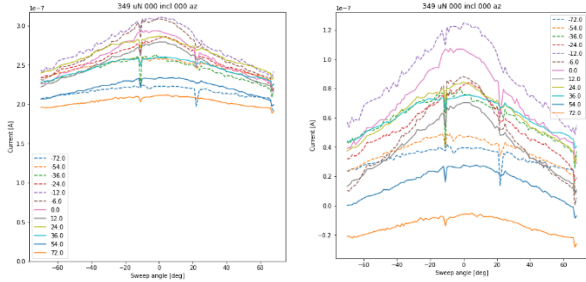
Figure 8: Current density over sweep angle, plotted by probe angle, for all probes, with idle offset (left) and with offsets subtracted (right)

Previous Faraday cup measurements of the plume of the IFM Nano – a comparable ion source – have shown that the current density becomes zero between 60 and 80 degrees (depending on the operating point), and that it approaches this limit linearly [15]. Accounting for the aforementioned offset, both these characteristics can be seen in the data of this test. Furthermore, the peak current density is approximately three times higher than in the aforementioned study, which correlates with the three times higher emission current (approx. 3 mA compared to 1 mA in [15]).

4. RESULTS

The presented results focus on information inferred from plasma diagnostic data. For colour plots, the lower limit is chosen slightly above zero, causing all negative and zero values to appear white, providing a stronger contrast along the edges.

4.1. Data examination and verification

Inspection of visualised data initially reveals two artefacts. The first is a trough in the centre, along the entire sweep. An example of this is given in Fig.9.
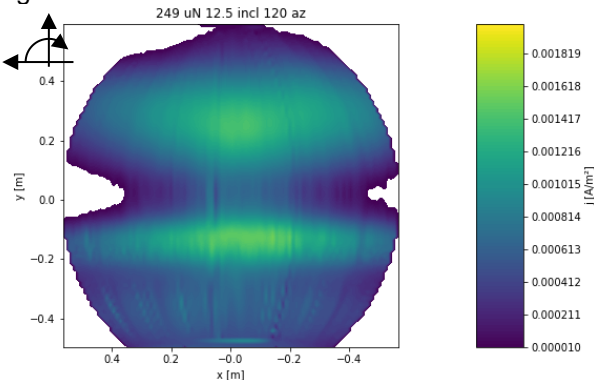
Figure 9: Example case showing a trough at zero elevation

Due to the consistency of the location of this observation across all operating points, in particular its independence of the azimuth of the thrust vector, it can be attributed to the measurement setup, most likely either to the signal conditioning unit or to the affected probe(s) themselves. Despite the artificial nature of this observation, the related data are kept in the presented results as they are.

Additionally, the data of some OPs show distinct strands of unusually high or low signal compared to data in the immediate proximity (example see Fig.10).
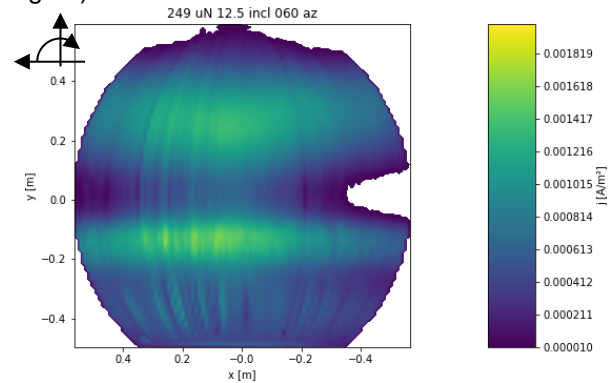
Figure 10: Example case showing amplified or weakened strands with a shape reminiscent of the diagnostic arm

From the shape of these strands, it is evident that they correspond to one data point of sweep angle measurements. They appear because scans may differ in their sampling of the sweep angle, which, when merging and averaging across multiple scans of the same OP, may cause individual samples to appear amplified or weakened relative to the rest of the scan data.

4.2. Probe type comparison

The measurements of the subject probe (ALTA) is qualitatively compared to a reference probe (FOTEC) located at the same angle on the other side of the mid-plane. This is done by plotting the raw data of these two probes over the sweep angle. Fig.11 shows that for an OP with an uninclined commanded thrust vector, the ALTA probe acquires a lower current than the FOTEC probe at a comparable location.
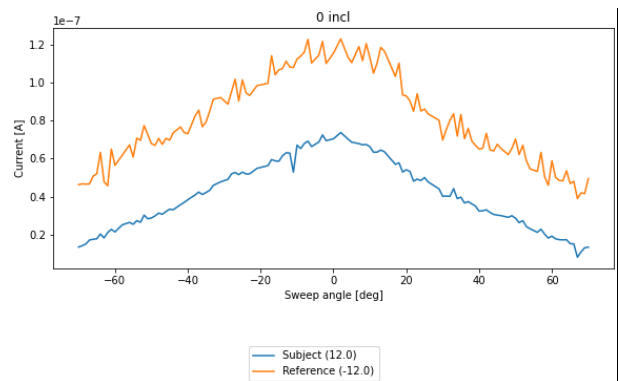
Figure 11: Raw current measured across sweep angle for the ALTA probe (blue) and a FOTEC probe placed on the opposite side of the beam (orange)

This pattern of a lower amplitude emerges consistently across OPs with an inclined thrust vector, as can be seen in Fig.12.
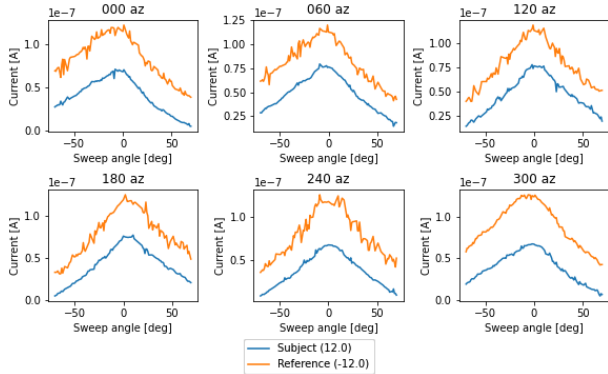
Figure 12: Raw current measured across sweep angle for the ALTA probe (blue) and a FOTEC probe placed on the opposite side of the horizontal mid-plane (orange) for a slightly inclined thrust vector (5°) at multiple azimuth angles measured clockwise around the thruster axis starting at the left horizontal, from top left to bottom right

Note here that in the first row second and third image, the beam is actually inclined towards the subject, yet the acquired current is lower than that of the reference, albeit by less than for an uninclined thrust vector. Meanwhile, the gap between the two increases when the beam is inclined away from the subject (ALTA probe).

4.3. Divergence angle

The divergence angle around the thrust vector is approximately 49° for all OPs. Note however that due to the limited field of view of the Faraday scans, the computation of this angle is an underestimation of the true divergence angle.

In comparison, Mühlich et al. [15] experimentally found a divergence angle of 63° for the IFM Nano, which is the precursor of the DUT. In a simulation of that device, they found a divergence angle of 49°.

4.4. Thrust vectoring

An excerpt of significant OPs is presented in the following. The colour scale is kept constant across all figures, allowing for further comparison. However this leads to noticeably less contrast for the lower thrust OPs. Fig.13 shows colour plots of the post-processed current density of OPs that have a thrust vector inclination of 12.5°, which is the highest inclination commanded during this in this campaign. However, these OPs have the lowest commanded thrust value, which is 249 µN.
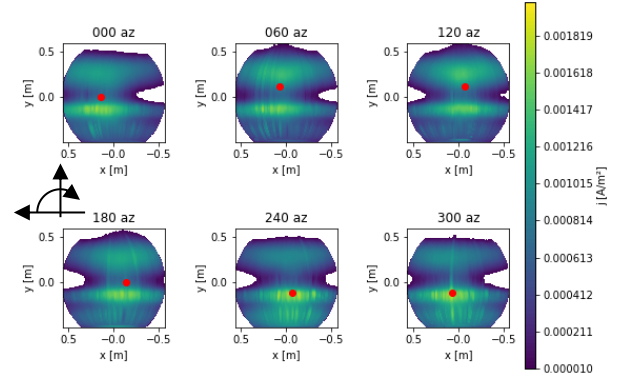
Figure 13: Ion current density over x and y as seen from the thruster, at 249 µN, 12.5° inclination, and various azimuth angles measured clockwise around the thruster axis starting at the left horizontal, from top left to bottom right (red dot marks commanded thrust vector)

Fig.14 shows the OPs that have a slightly lower thrust vector inclination (10°) while having an increased thrust (299 µN).
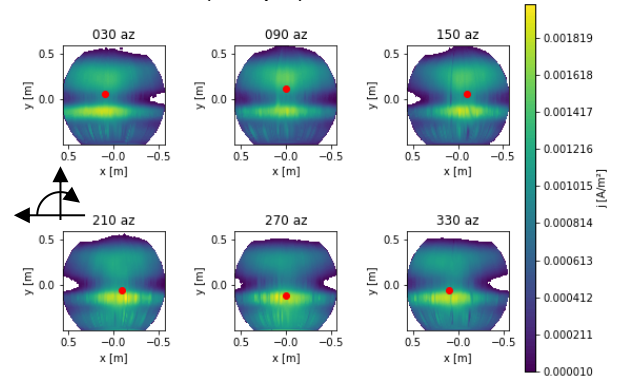
Figure 14: Ion current density over x and y as seen from the thruster, at 299 µN, 10° inclination, and various azimuth angles measured clockwise around the thruster axis starting at the left horizontal, from top left to bottom right (red dot marks commanded thrust vector)

Fig.15 shows the OPs with the highest thrust commanded during this test campaign (349 µN). However, the thrust vector inclination is reduced to 5°, which makes the skewed current density distribution less evident from the provided graphs.
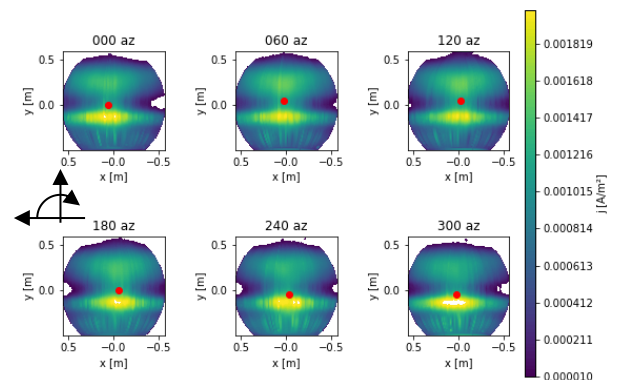
Figure 15: Ion current density over x and y as seen from the thruster, at 349 µN, 5° inclination, and various azimuth angles measured clockwise around the thruster axis starting at the left horizontal, from top left to bottom right (red dot marks commanded thrust vector)

5. CONCLUSION

The qualitative characterisation of the NANO AR³ FEEP propulsion system was completed successfully using the plasma diagnostics setup at the EPL. Specifically, the inclination of the ion beam without the use of moving parts was achieved and verified by means of Faraday cup data. The beam divergence is not measurably affected by the inclination of the beam, and it is comparable to the divergence angle obtained during a previous, independent study on a precursor model.

The ALTA Faraday probe designed for use with Xenon acquires a lower current than the FOTEC probes, which are designed for use with indium.

6. REFERENCES

[1] Pollard, J., & Welle, R. (1995, July). Thrust vector measurements with the T5 ion engine. In *31st Joint Propulsion Conference and Exhibit* (p. 2829).

[2] Scharlemann, C., Genovese, A., Schnitzer, R., Buldrini, N., Sattler, P., & Tajmar, M. (2009). In-FEEP endurance test for LISA PF. In *45th AIAA/ASME/SAE/ASEE Joint Propulsion Conference & Exhibit* (p. 5093).

[3] Merriam, E. G., Jones, J. E., Magleby, S. P., & Howell, L. L. (2013). Monolithic 2 DOF fully compliant space pointing mechanism. *Mechanical Sciences, 4*(2), 381-390.

[4] Bright, C. A., Tuttleb, S. L., Barracloughc, S. M., & Neelyd, A. J. (2016). *Fluidic Thrust Vector Control for Rendezvous Missions.* IAC-16-C1, IP, 9, x32006.

[5] Seifert, B., Buldrini, N., Hörbe, T., Plesescu, F., Reissner, A., Krejci, D., Friedhoff, P., & Lai, S. (2018). In-orbit demonstration of the indium-FEEP IFM nano thruster. In *Proceedings of 6th Space Propulsion Conference.*

[6] Krejci, D., Reissner, A., Seifert, B., Jelem, D., Hörbe, T., Plesescu, F., Friedhoff, P., & Lai, S. (2018, June). Demonstration of the ifm nano feep thruster in low earth orbit. In *4S Symposium, Sorrento, Italy.*

[7] Tajmar, M., Genovese, A., Buldrini, N., & Steiger, W. (2002). Miniaturized Indium-FEEP Multiemitter Design and Performance. *NanoTech 2002-" At the Edge of Revolution"*, 5718.

[8] Tajmar, M., & Scharlemann, C. A. (2011). Development of electric and chemical microthrusters. *International Journal of Aerospace Engineering, 2011.*

[9] Tajmar, M. (2011, September). Overview of indium LMIS for the NASA-MMS mission and its suitability for an In-FEEP thruster on LISA. In *Proceeding of the International Electric Propulsion Conference, IEPC-2011* (Vol. 9).

[10] Reissner, A. (2016). The IFM 350 Nano Thruster-Introducing very high Δv Capabilities for Nanosats and Cubesats. In *52nd AIAA/SAE/ASEE Joint Propulsion Conference* (p. 5044).

[11] Massotti, L., Gonzalez del Amo, J., Silvestrin, P., Krejci, D., Reissner, A., & Seifert, B. (2021). The Next Generation Gravity Mission and the qualification of the indium-fed mN-FEEP thruster. *CEAS Space Journal*, 1-16.

[12] Taylor, G. I. (1964). Disintegration of water drops in an electric field. *Proceedings of the Royal Society of London. Series A. Mathematical and Physical Sciences, 280*(1382), 383-397.

[13] Mühlich, N. S., Seifert, B., Ceribas, E., Gerger, J., & Aumayr, F. (2021, October). High-Precision Digital Faraday Cups for FEEP Thrusters. In *72nd International Astronautical Congress (IAC), Dubai.*

[14] Clough, R. W. (1965). Finite element stiffness matricess for analysis of plate bending. In *Proc. of the First Conf. on Matrix Methods in Struct. Mech.* (pp. 515-546).

[15] Mühlich, N. S., Seifert, B., & Aumayr, F. (2020). IFM Nano Thruster performance studied by experiments and numerical simulations. *Journal of Physics D: Applied Physics, 54*(9), 095203.